POLITECNICO
MILANO 1863

DIPARTIMENTO DI MECCANICA

mecc

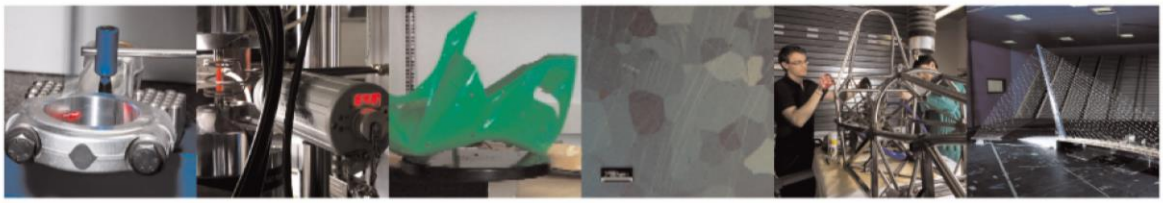

Al-Sn Miscibility Gap Alloy produced by Power Bed Laser Melting for application as Phase Change Material

Chiara Confalonieri, Elisabetta Gariboldi

This is a post-peer-review, pre-copyedit version of an article published in journal title. The final authenticated version is available online at https://doi.org/10.1016/j.jallcom.2021.160596

Al-Sn Miscibility Gap Alloy produced by Power Bed Laser Melting for application as Phase Change Material

Chiara Confalonieri[a]*, Elisabetta Gariboldi[a]
[a]Politecnico di Milano, Department of Mechanical Engineering, Via La Masa 1, 20156 Milan (Italy)
chiara.confalonieri@polimi.it, elisabetta.gariboldi@polimi.it
*corresponding author

Abstract

Alloys based on the Al-Sn system are Miscibility Gap Alloys consisting of two phases: a low-melting Sn phase and a high-melting Al phase. The two phases are almost immiscible in solid state, with minimal miscibility of Al in liquid phase just above the Sn-phase melting temperature. This situation allows the alloy to be used as a composite Phase Change Material, where the low-melting (active) phase (Sn) acts as the actual Phase Change Material, storing/releasing latent heat at each thermal cycle across its activation temperature, and the high-melting (passive) phase (Al) plays its main role in fast driving heat within the composite material, thanks to its high thermal conductivity. Thermal response of PCM composites is expected to be faster if the active phase is finely combined to the matrix. Moreover, if the active phase is embedded in the passive phase, leakage phenomena can be prevented and the continuity of the passive phase, acting as matrix, also allows residual structural properties to the composite above the temperature at which the low-melting phase is activated. In these conditions, the composite PCM can be considered as a form-stable composite material.
In this paper, the effect of rapid solidification has been investigated as a tool to get suitable microstructure of an Al-Sn alloy in view of its application as a composite PCM. The rapid solidification has been obtained by a Power Bed Laser Melting (also known as Selective Laser Melting) process. In the case of positive results for microstructure, the process will allow to overcome critical points in the manufacturing of composite PCM parts by powder metallurgy, mainly consisting in limitations on size and geometrical features of the parts.

Keywords: Composite Phase Change Material, Al-Sn, Miscibility Gap Alloys, Metal matrix composite, Rapid solidification, Power Bed Laser Melting

Highlights

- An Al-Sn based Phase Change Material was produced through Selective Laser Melting.
- Alloy microstructure is very fine and partially oriented in building direction.
- The anisotropy in thermal conductivity can be beneficial for the final application.
- Thermal response agrees with that of Al-Sn alloys produced by other PM methods.

1. Introduction

The generation of a heat surplus under specific conditions is a critical issue in many engineering applications as well as in many industrial plants. In both cases, a convenient way to deal with it is by using Phase Change Materials instead of active cooling systems [1]. These materials are suitable to perform the so-called 'Thermal Energy Storage', when as much as possible of the heat surplus of the system must be stored to be used later (e.g., solar energy power plants). Alternatively, heat can be used for 'Thermal Energy Management', when at least part of the heat surplus generated during transients has to be removed to avoid to reach excessive temperatures or excessively rapid

heating or cooling rates (e.g. portable electronics) [1]. Phase Change Materials (PCMs) are functional materials, that exploit a phase transition which changes one or more material properties. In the case of thermal applications, PCMs can store the thermal energy associated to a phase transition, i.e., the latent heat of transition, and release it when the transition is reversed. A significant advantage with respect to an active cooling system is that their action depends only on the material itself and not on the applied heat flow or external flow source [1].

The range of application of a PCM is mainly defined by latent heat and temperature of the transition. Other properties must be considered to meet project requirements, concerning thermal, physical, dynamic, chemical, economic and technical performance, as discussed by Wei et al. [2]. In this framework, the most studied and applied PCMs are organic materials and inorganic compounds (e.g., molten salts). On the other hand, metals are usually less considered; according to Fleisher [1] and Mohamed et al. [3], this is due to their low latent heat per unit mass. However, metals have several advantages, like high application temperatures, high thermal conductivity and high density, which results in high heat per unit volume [2–4].

Metallic PCMs can be pure metals or alloys, which usually undergo solid-liquid or solid-solid transitions [5,6]. According to Wei et al. [2], the most promising metallic PCMs are Al alloys, due to their transition temperatures, suitability for many applications, and good corrosion resistance. In the case of solid-liquid transition, it is necessary to choose a proper container material to avoid liquid corrosion and consequent PCM contamination as well as container damage [2]. For this reason, the metallic PCM is usually encapsulated through a mechanical or electroplating approach [5]. However, oxidation or corrosion due to interactions between PCM and container can occur especially at high temperature, compromising performance and functionality of the system; moreover, thermal conductivity of the system can be low [5]. Another way to obtain PCM relies on designing composite materials (C-PCM), consisting of an active phase undergoing the transition (i.e. the actual PCM) and a passive matrix which does not change in the entire range of working temperature [7]. The passive phase can have several roles, like enhancing thermal conductivity, embedding the active phase without the need of encapsulation and providing structural or other functional properties [7]. When the matrix has the last two roles, the PCM can be defined as ‘form-stable’ [8]. To obtain a metallic C-PCM exploiting a solid-liquid transition, the constitutive phases must not interact in solid state as well as when the active phase is molten, to keep a constant composition. An effective solution is the use of Miscibility Gap Alloys (MGAs), as suggested by Sugo et al. [9]. These systems are often applied in bearing materials and, so, production processes are well known.

An ideal PCM candidate based on MGA is the Al-Sn alloy, which was proposed by Sugo [9] and is considered also in this study. The phase diagram of this alloy shows an eutectic point with around 99.5% in mass of Sn at 228°C [10]; since the eutectic composition is almost pure Sn and the eutectic temperature is very close to pure Sn melting temperature (232°C), it is possible to assume that the alloy has a miscibility gap. Thanks to the frequent use of Al-Sn as the base alloy system for bearing materials, several production processes were considered and studied. Similarly to form-stable PCMs, bearing materials require a homogeneous dispersion of the soft, lower melting phase (e.g. Sn or Pb) in the Al matrix; this microstructure proved to improve hardness, friction and wear behaviour [11]. However, a common issue with MGAs is that conventional casting results in the high melting phase surrounded by the low melting phase, which is opposite to the desired microstructure [9,12]. High density difference and mutual immiscibility of system components are possible causes of this phenomenon [12]. Therefore, it is important to select carefully a suitable production process; in the following, a brief review of production process applied to Al-Sn based systems is presented.

Powder metallurgy processes are widely applied to produce bearing materials, since powder mixing followed by compression and sintering can embed Sn in the Al matrix. Zhu et al. conducted several studies on the effect of ball milling and sintering temperature and time on Al-Sn alloys [11–14]. They observed that this approach allows to obtain a fine microstructure with nanometric Sn particles embedded in Al, resulting in very good hardness and wear resistance. Powder metallurgy processes to obtain Al-Sn based PCMs were applied by Sugo et al. [9] as well as in previous works by the authors [4,15,16]. This method proved to be quite effective to produce form-stable metallic PCMs, with isolated active phase particles.

Cold-spray deposition has been applied to deposit the Al-Sn layer directly on components, usually made of steel or Al alloys. For some aspects, this process can be considered similar to powder metallurgy, since the powder blend is compacted without melting and then sintering is necessary. For example, Ning et al. applied a cold-spray deposition process, in which gas atomized Al-Sn alloy powders (5-10 mass% Sn) were deposited on the steel substrate at high speed and temperature lower than melting one [17]. Deposition was followed by annealing at different temperatures, between 150°C and 300°C for 1 hour. Low porosity, good bonding and high hardness (73-74 HV) were obtained.

Another possible approach is using casting processes which involve specific strategies to avoid Sn segregation at Al grain boundaries, like rapid solidification of the melt and the addition of grain refiners and alloying elements. Stuczyñski (1997) developed a foundry technique to produce Al-Sn ingots to be used as input material for bearings [10]. His method is based on stirring continuously the metal bath during melting in order to avoid segregation and selecting a suitable ingot casting method to ensure fast solidification. Regarding the latter, Stuczyñski observed that continuous or semi-continuous casting gives better results than die casting, if economic conditions are satisfied. In addition, a grain refiner (AlTi5B1) was added to improve Sn homogeneous distribution and the metal bath was degasified to reduce the formation of solid non-metallic inclusions. Final steps in Al-Sn ingot production were cold work and annealing at 350°C for 4 hours. More recently, in 2013, Chikova et al. studied how to improve a traditional casting method for an Al-50 mass% Sn based on heating molten Al-Sn alloy at 700°C and then cooling rapidly (0.2°C/s) [18]. Overheating the melt induces an irreversible transformation of the molten alloy in an homogeneous state, which is kept in the solid state thanks to rapid solidification [18]. The proposed new method involved increasing the overheating temperature to 1150°C and the cooling rate to 4°C/s, as well as adding Ti (0.06 mass%) or Zr (0.1 mass%) as alloying elements. The best results were obtained for heating at 1150°C with cooling at 4°C/s and addition of Zr, reducing Young modulus, hardness and residual stresses, so improving metal forming of the alloy ingot.

Rapid solidification is exploited also in thermal spray processes, which are used to deposit Al-Sn layer directly on component. The difference with respect to the above-mentioned cold-spray process is that powders are melted before deposition. Makhatha et al. investigated rapid solidification through a laser alloying technique, applied on Al-Sn alloys with 75-50-25 mass % of Sn [19]. Laser scanning speed was 0.6-0.8 m/min. Very good performances were observed for hardness (above 100 HV), wear and corrosion resistance. On the other hand, Marrocco et al. tested a high-velocity oxyfuel (HVOF) thermal spray process [20]. The alloy contained also 1 mass% Cu and 2 mass% Ni or 7 mass% of Si. Rapid solidification resulted in the deposition of an Al-Sn based layer with low porosity directly on a steel strip. Post deposition heat treatment at 300°C was conducted for 1 to 5 hours, followed by air cooling. Sn particles of micrometric and submicrometric size were observed. The sample containing Si showed the best wear resistance.

Another conventional rapid solidification process is melt spinning. An ingot with homogeneous composition is molten and injected on the outer surface of a cooled rotating roller, usually under Ar atmosphere. The cooling rate is in the order of 10^5-10^6 K/s [21]. This process is frequently used

in industrial production of thin sheets of amorphous or quasi-crystalline metals, known also as metallic glasses. On laboratory scale, many authors, like Kim and Cantor [22] and Zhang et al. [23], produced ribbons of Al-Sn alloys to study heterogeneous nucleation of Sn particles embedded in Al matrix. The resulting microstructure consist of a fine columnar structure of α-Al and Sn particles that can be "bulk" (> 10 µm), agglomerated at grain boundaries or nanometric and homogeneously distributed in the Al matrix [21–24].

In this paper, a rapid solidification approach has been considered as a method to obtain an Al-Sn alloy suitable to be applied as PCM. The selected process was Selective Laser Melting (SLM, also referred as Powder Bed Laser Melting). In this process, a simple mixture of powders (in the present case, 60% Al and 40% Sn in mass) is locally melted and then rapidly solidified, leading to building and shaping specimens of alloy by stacking layers of consolidated alloy along a specific direction. The potential of this approach is the possibility to obtain a metallic C-PCM, characterized by a fine microstructure thanks to the rapid solidification, with the design freedom allowed by an additive manufacturing process. The authors also aimed at comparing its thermal response and microstructural stability during simulated service as C-PCM materials with their previous results of [4,15,16] on an Al-Sn MGA with the same composition produced by powder metallurgy methods not involving solidification. Material characterization focused on ~~i~~ microstructural and mechanical properties, as well as thermal and functional properties that are important for the application as PCMs.

2. Materials and Methods.

Pure Al (ECKA Granules Germany GmbH) and pure Sn (STAGNO 106, Metalpolveri S.r.l) powders were mixed to obtain a blend with 20% volume of Sn, corresponding to about 40% in mass. Previous works by the authors focused on alloys with the same composition, but different production processes [4,16,25]. Both powders had high purity (>99.7% in mass). The purchased Al powder had grain size approximately <45 µm, while Sn powder had a wider size distribution with also coarser particles (>106µm: 0.1%, >45µm: 15-45%, <45µm: 55-85%). Before the mixing processes, powders were sifted with a 63 µm sieve, to remove coarse particles and agglomerates. Then, they were mixed for 1 hour at 20 rpm at room temperature, in mass ratio 60/40 Al/Sn (corresponding to volume ratio 80/20). Two sets of samples have been produced, using a Renishaw additive manufacturing system AM 250 equipped with a Reduced Build Volume apparatus (powder bed 90 mm x 90 mm), operated in argon atmosphere (O < 1000 ppm). Among a series of tentative samples produced by varying process conditions [26], the two with the following parameters (called S1 and S2) were considered for the present paper, focused on the microstructural features and on its development during service as Phase Change Materials. The laser power was fixed to 200 W and the exposure time to 160 µs. The layer thickness of the powder bed was 25 µm. Meander scanning strategy was applied, rotating the scanning direction of 67° after each layer completion. The two samples of Al-Sn MGA showed in this work were produced with the same point distance (100 µm), i.e., distance between two consecutive laser pulses. On the other hand, the distances between the parallel adjacent scanned tracks, i.e., hatch distance, were different (80 µm for S1 and 100 µm for S2) and, as a result, also the specific energy (*E*) applied to the powders changed. The specific energy (also referred as volumetric energy density, and expressed in J/mm^3) was calculated using the following equation, approximating the scanning speed ~~v~~ as the ratio between point distance (i.e., distance between two neighbour points exposed to the pulsed laser) and exposure time (i.e., time of a laser pulse) since a pulsed laser was used (Equation 1):

$$\underline{E} = \frac{P}{d_h \cdot v \cdot l} \approx \frac{P \cdot t_{exp}}{d_h \cdot d_p \cdot l} \qquad \text{(Equation 1)}$$

where P is the laser power, d_h is the hatch distance, v is the scanning speed, l is the layer thickness, t_{exp} is the exposure time and d_p is the point distance. Values for $\underline{E}$ were thus 160 and 128 J/mm^3 for S1 and S2 samples, respectively.

Both S1 and S2 samples were produced as parallelepipeds, with dimensions of 8x4x8 mm and 40x5x9 mm respectively~~;~~. Once removed from the building (not heated) platform, samples were cut in smaller regular pieces for further testing. Mounted samples were ground with abrasive papers and then polished with diamond suspensions and silica suspensions down to 0.5 µm.
The specimens were tested with the same simulated service conditions used in previous investigations on Al-Sn alloys used as composite PCMs. This simulated service consisted of thermal cycles between 180°C and 280°C, with heating/cooling rate of about 25-28°C/min. 100 thermal cycles were carried out with Ar flux, to avoid Sn oxidation in the temperature range where it is molten.
Characterization of the MGA alloy produced by SLM was carried out before and after simulated service, including the analysis of microstructure, mechanical properties and thermal behaviour.
In microstructural characterization, both Optical Microscopy (OM, Nikon Eclipse LV150NL) and Scanning Electron Microscopy (SEM) were used to evaluate materials features at different scale-length. Since in both cases phase contrast is sufficiently high, no chemical etching of the polished surfaces was performed. ~~a~~ SEM analysis were carried out using either a W-SEM (Zeiss EVO 50) and a high-resolution Field Emission Gun SEM (FEG-SEM, Zeiss Sigma 500). Further, Electron Back Scattered Diffraction (EBSD), using an Oxford Instrument C Nano EBSD detector in the FEG-SEM, allowed to analyse grain orientation of S2 sample in as-produced conditions; an area of 38.0x15.8 µm was scanned with step size of 58.3 nm.
Quantitative evaluation and analyses of microstructural features ~~has~~ have been carried out using ImageJ software (in the Fiji distribution) [27], under the assumption suggested by Underwood that the volume fraction of a phase is equal to its area fraction [28]. An analysis of pore morphology was conducted on OM images of the whole central section parallel to building direction. The considered shape descriptors are particle area, equivalent diameter, circularity and aspect ratio. The equivalent diameter is computed from the area considering the particle as circular. Circularity shows if the particle is round and smooth (value tends to 1) or it has irregular surface and/or elongated shape (value tends to 0). Finally, aspect ratio is the ratio between the major and minor axis of the fit ellipse [29,30]. Sample density was calculated from porosity fraction measured from OM images of the whole section parallel to the building direction, considering that pores increase material volume with a negligible increase in mass.
The preliminary analysis of the mechanical behaviour of the material was carried out by means of Vickers microhardness (HV). HV was measured along the sample direction parallel to the building direction, using a Future-tech FM-700 microhardness tester with 4.91 N applied load and 15 s dwell time, with 5 repetitions.
Thermal energy storage for the manufactured C-PCMs was evaluated through Differential Scanning Calorimetry (DSC) tests, using a TA Instruments DSC 2010 V4.4E. Samples of mass of about 10 mg corresponding to about 3.3 mm^3 (slightly lower for thermally cycled specimen), placed in Al crucibles were thermally cycled twice in inert Ar atmosphere. These were heated at 20°C/min from -50°C to 320°C, held 1 min at 320°C and then cooled to RT with cooling rate set to 20°C/min. This thermal history should have ensured complete solid/liquid phase transition of Sn.

Experimental values of density and thermal properties were compared with theoretical values for Al-40%Sn (mass percentage) obtained with thermodynamic calculations (Thermo-Calc Software TCAL5 Al-alloys database, [31,32]).

Finally, the effective thermal conductivity of different regions in the alloy was estimated with Lattice Monte-Carlo (LMC) approach, using a software developed by our research group and presented in a dedicated paper (Li [33]). The same numerical method was applied previously on Al-Sn alloys by the authors [34] and by Rawson et al. [35]. Its advantage is the possibility to simulate the effective thermal conductivity of a multiphase material taking into account the actual microstructure. In the case of a binary system (like Al-Sn), a micrograph of suitable magnification is binarized, i.e., each pixel is converted to black or white according to a threshold defined with the Otsu's method [36], resulting in a matrix of size n x m with elements 0 and 1 only, the so-called *lattice*. Nodes with value 0 belong to the *matrix* and nodes with value 1 belong to the *inclusions*, in the present case Al and Sn respectively; each phase is characterized by its thermal conductivity (237 W m^{-1} K^{-1} for Al, 66.6 W m^{-1} K^{-1}, [37]). Thermal conductivity is related to the probability of a "virtual" energy *particle* to move in the lattice randomly with a set of successful or unsuccessful *jumps* into the near-neighbour node in a certain time, i.e., time for each jump attempt multiplied by the total number of jumps. The calculation of this probability is repeated for a specified number of particles. At the end, three values of conductivity are calculated: in vertical direction (k_1), in horizontal direction (k_2) and the average between the two (k_av). In the present paper, areas of size 110*110 pixel, corresponding to 143 μm^2, were chosen to analyse thermal conductivity in representative regions; a high magnification was necessary to have a good resolution of phases and the sampling of 10 small areas per each sample allowed to have a statistical analysis as well as a relatively short simulation time (around 1:30 hours). The number of particles was set equal to the number of nodes (110*110 = 12100) and the number of jumps was set to 10000, which is a suitable value for a lattice of this size according to Li [25]; the latter assumption was verified repeating the simulation for all areas of S1 sample increasing the number of jumps (5, 100, 1000, 10000) without modifying the other parameters. The simulation was repeated 3 times for each area to ensure statistically representative results. In the present work, the use of LMC simulation aimed to understand the local effect of different phase distributions on isotropy of the thermal conductivity of the composite. Results are compared with upper and lower bounds for thermal conductivity ($k_{c,u}$ and $k_{c,l}$, respectively) obtained with the rule of mixture (Equation 2 and Equation 3 [38]) as function of Sn volume fraction (v_{Sn}):

a) upper-bound expression

$$k_{c,u} = k_{Al}v_{Al} + k_{Sn}v_{Sn} = k_{Al} + (k_{Sn} - k_{Al})v_{Sn} \qquad \text{(Equation 2)}$$

b) lower-bound expression

$$k_{c,l} = \frac{k_{Al}k_{Sn}}{k_{Al}v_{Sn} + k_{Sn}v_{Al}} = \frac{k_{Al}k_{Sn}}{k_{Sn} + (k_{Al} - k_{Sn})v_{Al}} \qquad \text{(Equation 3)}$$

where k_{Al} (237 W m^{-1} K^{-1}) and k_{Sn} (66.6 W m^{-1} K^{-1}) represent thermal conductivity of Al and Sn respectively [37], while v_{Al} and v_{Sn} are the volume fractions of Al and Sn, the sum of which is equal to 1.

3. Results

3.1. Macrostructure

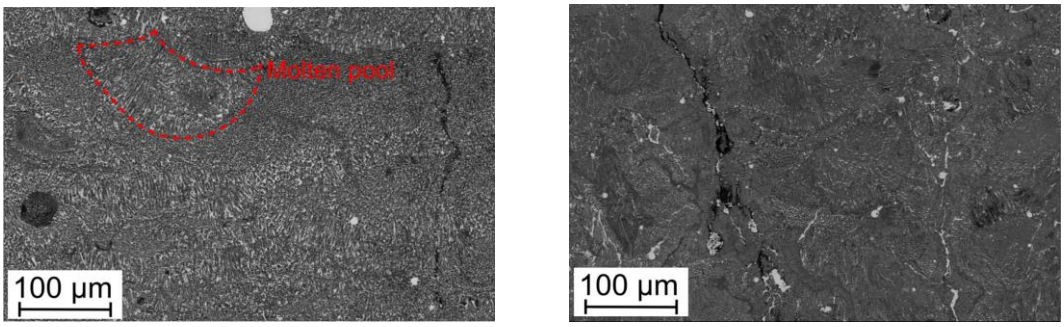

a) b)

Figure 1. Low-magnification SEM micrographs of as-produced samples: S1 (a) and S2 (b). Metallographic sections are parallel to building direction (here vertical).

The microstructure of the Al-40mass%Sn alloys can be clearly observed in relatively low magnification SEM micrographs shown in Figure 1a and Figure 1b for S1 and S2 samples, respectively. Both specimens ~~were~~ are in as-produced condition and cut on metallographic section parallel to the building direction (vertical in images). Due to Z-contrast, Al is dark-grey and Sn is white, while the darkest areas correspond to discontinuities (pores or cracks). For both samples, especially for S1, tracks of molten pools are visible as lighter horizontal bands in these low-magnification micrographs. Further, the macrographs show almost spherical pores and cracks developing vertically. The latter have more or less separated surfaces (compare Figure 1a to Figure 1b) and, in some cases, part of the crack is filled with Sn (e.g., the right-side one in Figure 1b). Cracks develop along building direction with small deviations when they cross porosities, mainly in the central part of the sample. The crack network observed on horizontal sections of the samples suggests a columnar macrostructure with hexagonal section. On the other hand, pores formed all over the sample volume, some of them located at crack tip or along a crack.

The presence of pores and cracks on the sample was characterized by Image J. The cracks distribution ~~was~~ is quantified by means of their average distances, considering 5 parallel lines along the thickness of the sample, perpendicularly to building direction, and measuring the mean crack distance. Even if cracks tend to concentrate at the centre of the sample, their average distance is 0.918 mm in S1 and 0.677 mm in S2. S2 sample is thus characterized by a higher crack density. Pores ~~were~~ are quite uniformly distributed in S2, but in S1 their number and size increase, especially close to the lateral surfaces, with an overall lower porosity area fraction (7.4%) compared to S2 (13.3%). Qualitatively, the pore density in S1 sample increases with build-up height. The specimen ~~density was~~ densities computed from these values ~~as~~ are 3.36 g/cm^3 and 3.23 g/cm^3 for S1 and S2 samples, respectively.

Comparing results of image analysis shown in Table 1, it is possible to observe that aspect ratio and circularity are quite similar for both samples. The values indicate that pores are quite circular and smooth; considering that they have similar shape also in transversal micrographs, it is possible to assume that in 3D they have spherical shape. Concerning size, pores in S1 sample are generally bigger than in S2 sample (+ 9.38% considering the mean area); this difference is more significant for big pores (about 5%) than for small pores (less than 1%). On the other hand, S2 sample has more pores: 73/mm^2 compared to the 51/mm^2 for S1.

Pores in S1 sample	*Pores in S2 sample*

	Area [μm²]	Equivalent diameter [μm]	Circularity	Aspect ratio	Area [μm²]	Equivalent diameter [μm]	Circularity	Aspect ratio
Mean	1743.28	47.11	0.73	1.72	1579.81	44.85	0.72	1.76
Max	50523.14	253.63	1.00	7.35	48109.38	247.50	1.00	7.70
Min	150.82	13.86	0.20	1.00	149.84	13.81	0.20	1.00
Mode	150.82	13.86	1.00	1.37	149.84	13.81	1.00	1.37

Table 1. Size and shape descriptors of pores

Higher-magnification micrographs in Figure 2a-b show the fine distribution of the two phases, where Sn is found at Al grain boundaries. Both micrographs show the melting pool inner and boundary regions.

Focusing on Sn distribution, it can be found both in a fine network around Al and in coarse isolated particles. The high-energy S1 sample (Figure 2a) clearly displays coarser structure. Sn phase has a minimum thickness of the order of 0.5-1 μm, surrounding Al grains 2-3 μm thick and elongated up to the extension of the melting pool (in Figure 2a, the maximum vertical length is about 25 μm). Sn particles tend to coarsen close to or in inter-pass regions. Further, there are regions in which Sn particles are still fine, but not elongated in a specific direction in the micrograph, resulting in a more isotropic structure. Finer and slightly different features for Sn particles can be observed in Figure 2b for S2 sample. Elongated particles are present as well, but they are thinner and less in number. In the same regions, Sn particles with size around 1 μm can be found; higher magnification micrograph of this area is shown in Figure 4b. Further, coarser Sn particles, mainly located close to inter-pass region and slightly elongated in solidification direction, with maximum length up to 3 μm are observed.

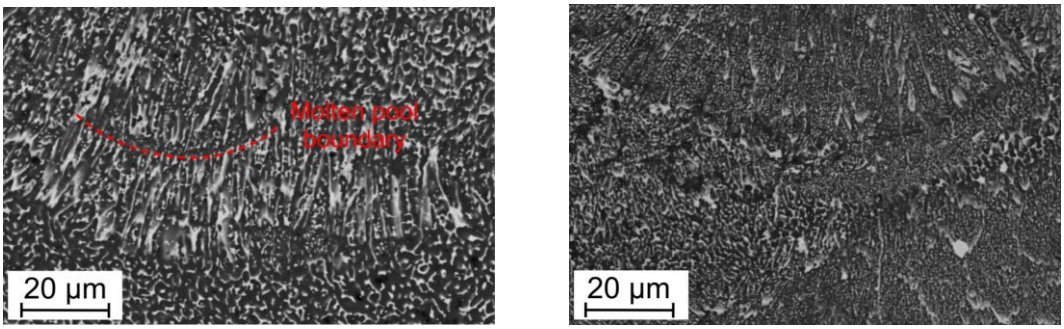

a) b)

Figure 2. FEG-SEM micrographs of as-produced samples: S1 (a) and S2 (b). Metallographic sections are parallel to building direction (here vertical).

Focusing the attention on coarse isolated Sn particles, which can be observed in both samples, even if in lower amount in S1 sample (see Figure 1), some of them are not completely filled by Sn phase. Examples are given in Figure 3 micrographs, taken with secondary electron probe and clearly showing the inner regions of the pores. Thus, ~~It~~ it can ~~thus~~ be generally observed that pores are partially filled by elongated columns of Sn protruding from pore surfaces (Figure 3b) and partly forming a compact Sn layer at pore surface (Figure 3a). For a similar pore size, the protruding Sn particles in the pore are much finer and filament-like in S2 sample, corresponding to its refined cell structure (Figure 3b).

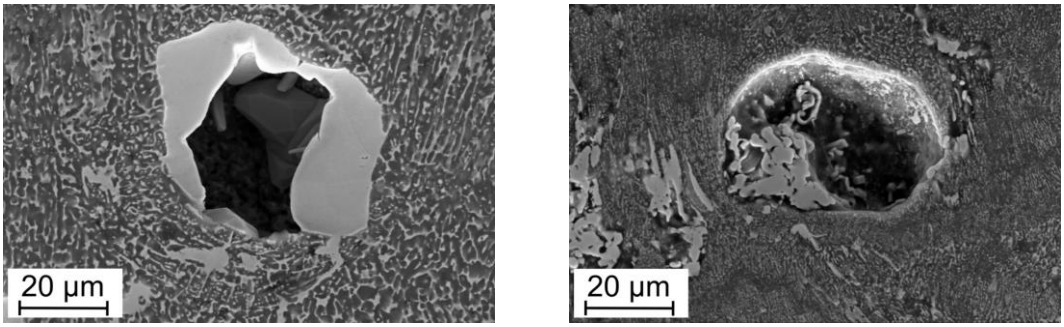

a) b)

Figure 3. Pores with Sn inside from S1 (a) and S2 sample (b)

EBSD analysis of as-produced samples were carried out on selected areas to investigate presence and orientation of both Al and Sn grains and the existence of orientation relationship between them, as shown by Kim and Cantor for an Al-Sn alloy produced through melt spinning [22]. Representative results are here shown for S2 sample, in a narrow analysis area of the metallographic section shown in the same Figure 4a.

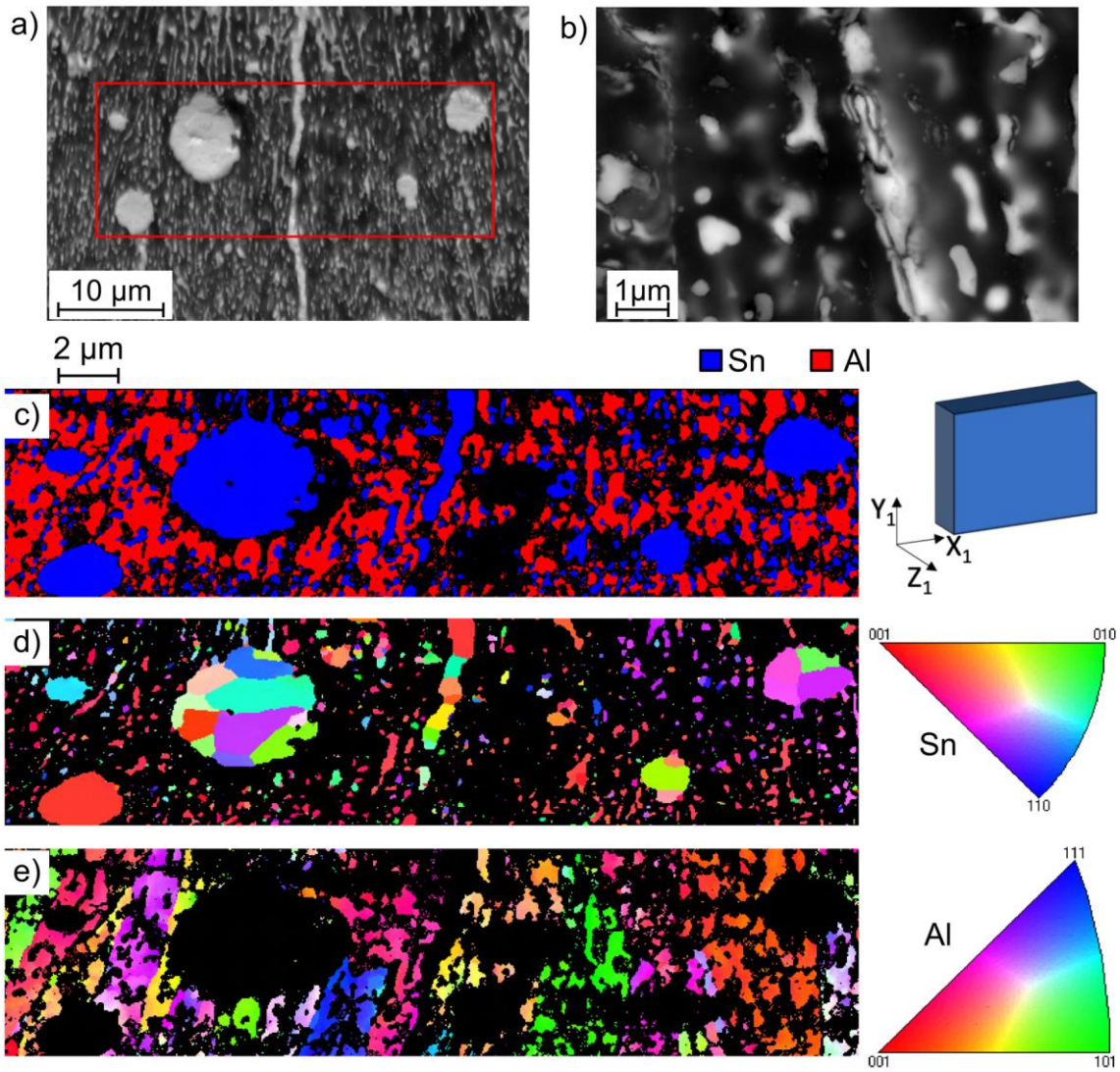

Figure 4. Small area of S2 sample shown tilted of 70° for EBSD analyses (a), containing both fine and coarse Sn particles as well as a thick elongated region of accumulated Sn. High magnification of a Sn-filled crack (b). EBSD results in Y_1 direction: phase map (c) with Sn in blue and Al in red,

Inverse Polar Figures (IPF) for Sn (d) and Al (e). In the sample reference system, Y_1 axis is parallel to building direction and Z_1 is perpendicular to sample surface.

Even if the phase identification in Figure 4c shows that indexing is not complete, it can be clearly observed that Sn (in blue colour) lays in coarse particles, in a thick elongated region and partly in particles of sub-micrometric size. The orientation maps of Sn phase show that sub-micrometric Sn particles have in general similar orientations (Figure 4d), while particles with equivalent diameter greater than 1 µm, typically include multiple grains with widely different orientation, for which no inter-correlation nor correlation to the surrounding Al structure was observed. The same can be observed for the Sn-elongated region in the middle of Figure 4d. In addition, a very high magnification micrograph of one Sn-filled cracks (Figure 4b) shows that Sn can display both cracks at Al interface and inner cracks resulting in elongated particles with thickness lower than 100 nm. Concerning Al grains orientation (Figure 4e), EBSD map consists of "vertical stripes", each corresponding to a cellular structure. The presence of hues inside of the stripes indicates grain inhomogeneities. Moreover, it can be noticed that the crack filled with Sn lays between two differently oriented elongated grains.

After 100 thermal cycles simulating service, the microstructure changes significantly in the phase distribution. The nearly hexagonal columnar structure suggested by the crack network is clearly visible in these samples. Formation of new cracks with respect to as-build conditions was not observed. The comparison between metallographic sections parallel to building direction before (Figure 1a-b) and after thermal cycles (Figure 5a-b) shows that deposition tracks are less evident after cycling. Further, a tendency of Sn to form coarser structures and fill discontinuities is clear for both the investigated samples.

Micrographs of sample sections perpendicular to building direction (Figure 5c-d) show that Sn filled to higher amount cracks and pores. Further, a sort of "beachmarks" underlying a wavy concentration of Sn can be observed at the external part of the coarse columnar structure surrounded by cracks. Within them, Sn content is generally low with extremely fine Sn particles (Figure 6a). The inner regions of columnar structures are characterized by Sn-rich areas where microstructural features, even if coarser, are similar to those of as-produced samples (Figure 6b). This phenomenon can be noticed also in sections parallel to building direction (Figure 5a-b) especially for S2 sample. Moreover, thermal cycles caused some Sn leakage from the sample, and the corresponding formation of almost spherical particles in external surfaces which progressively increased in size becoming visible at very low magnifications.

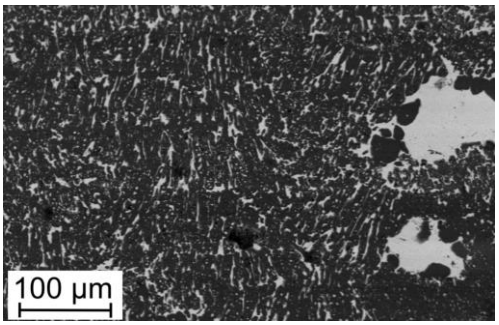

a)

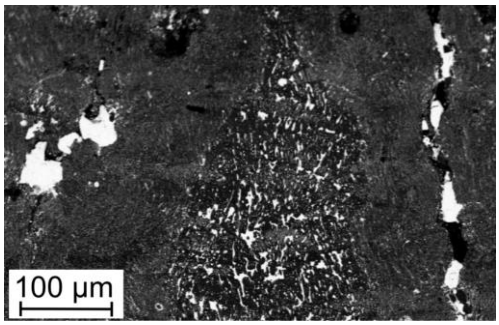

b)

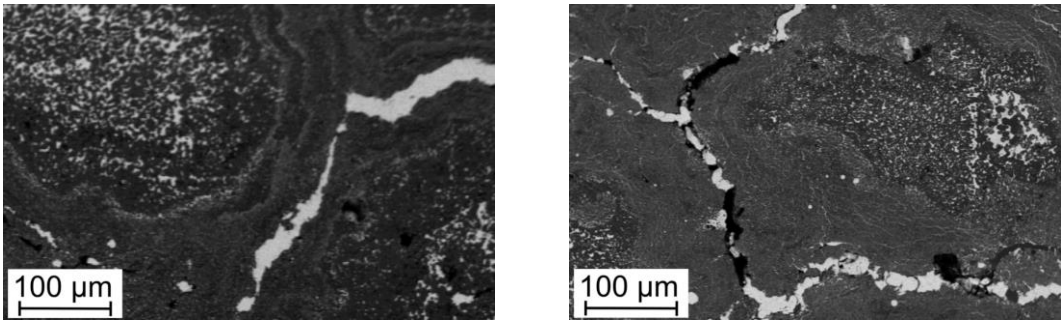

c) d)

Figure 5. W-SEM micrographs of S1 and S2 samples after simulated service: section parallel to building direction (a, b) and section perpendicular to building direction (c, d)

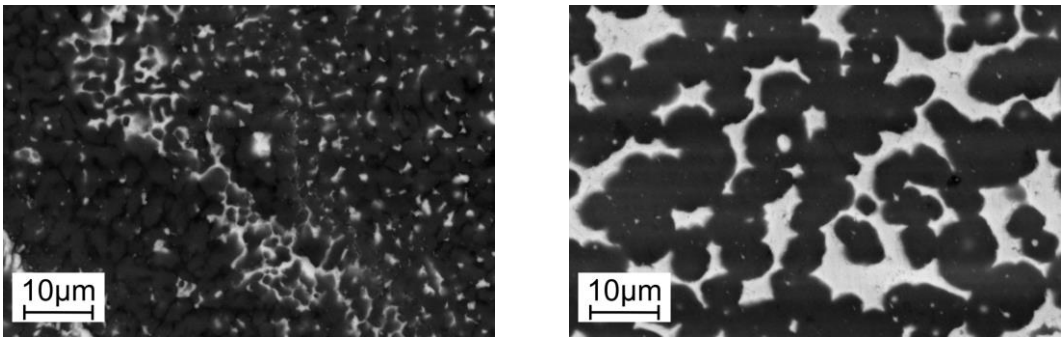

a) b)

Figure 6. W-SEM micrographs of S1 sample (section perpendicular to building direction) after simulated service at high magnification: (a) Sn-poor region, (b) Sn-rich region.

3.2. Vickers microhardness

Results of Vickers microhardness tests before and after simulated service are reported in Figure 7. Hardness values are generally around 30 HV, except for S2 sample in as-produced conditions, which reaches more than 40 HV. Standard deviation is quite large, especially for S1 sample after thermal cycles.

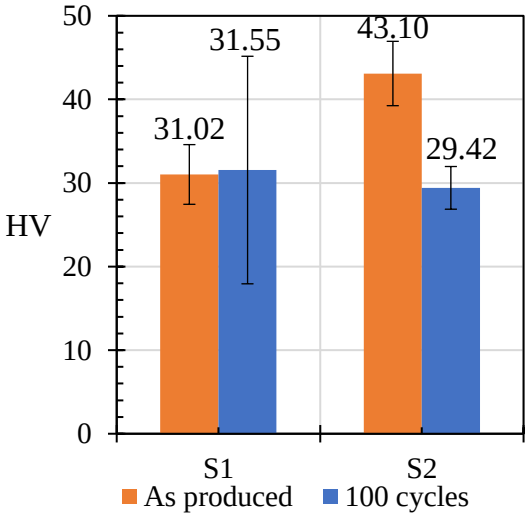

Figure 7. Vickers microhardness (HV) results for both samples, before and after 100 cycles simulating service (average over 5 measurements).

3.3. Thermal properties

3.3.1 Thermal storage

The thermal storage response of the materials was derived from DSC curves showing heat flow as function of temperature and presented in Figure 8 and Figure 9 for S1 and S2 sample, respectively. The endothermic (downward in plots) melting peaks of the two sample always occur at temperature (T_p) very close to that of pure Sn melting temperature (232°C). In addition to this peak, the only observed for the two DSC cycles performed on as-produced samples, another peak appears a couple of degrees before the main peak in DSC cycles performed on specimens previously subjected to 100 thermally cycles. Notwithstanding this, the transition temperature interval is always about 20°C.

The exothermic (upward) solidification peak occurs at lower temperature and in a more complex way. In both samples, the curves referred to the two DSC runs on as-produced samples display the first peak at T_p of about 220°C. The second broad peak is observed in the temperature range from 140°C to 113°C for S1 sample, and from 156°C to 70°C or 100°C in the first and second cycles for S2 sample, respectively. After 100 thermal cycles simulating service, the solidification conditions become more complex: the height of the solidification peak at 220°C clearly decreases with only slightly changes from the first to second cycle. The low-temperature region is smoother for S1 sample, while S2 sample shows changes in the number of peaks as well as in their temperature.

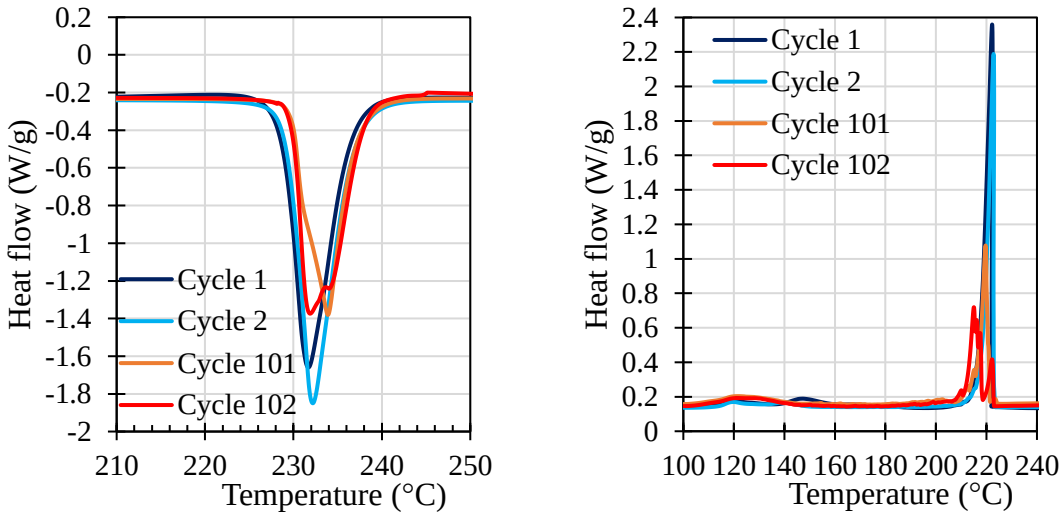

Figure 8. DSC curves of S1 sample: melting peak (a) and solidification peaks (b)

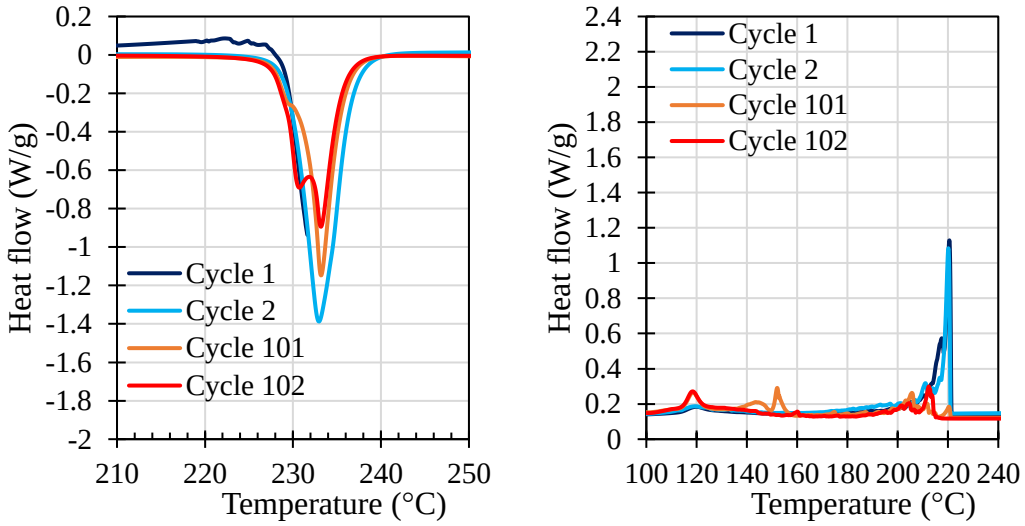

Figure 9. DSC curves of S2 sample: melting peak (a) and solidification peaks (b)

The above DSC curves were compared to additional ones (Figure 10) carried out on pure Al and pure Sn powders in order to check if the second solidification peak was related to an instrumental error, some impurities or to the fine microstructure of the Al-Sn alloy. Al curve did not show any peak, as expected. On the other hand, Sn had a single melting peak and multiple solidification peaks, two starting around 215°C and a broad one with T_p at about 140°C.

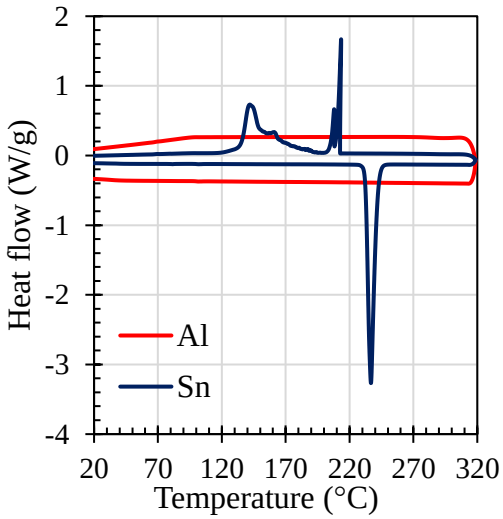

Figure 10. DSC curves of pure Al and pure Sn powders

The energy associated to the phase transition was calculated as the area of melting/solidification peaks in the curves of heat flow as function of time. Results for each sample, before and after thermal cycles, are reported in Figure 11; these values are the average of the enthalpy measured in each of the two cycles of the DSC test. When multiple solidification peaks were observed (both in case of Al-Sn alloy and pure Sn), if the area of all the solidification peaks is summed, the resulting value is close to the value of melting enthalpy. The reduction of stored energy after thermal cycles simulating service is around 30% for both samples.

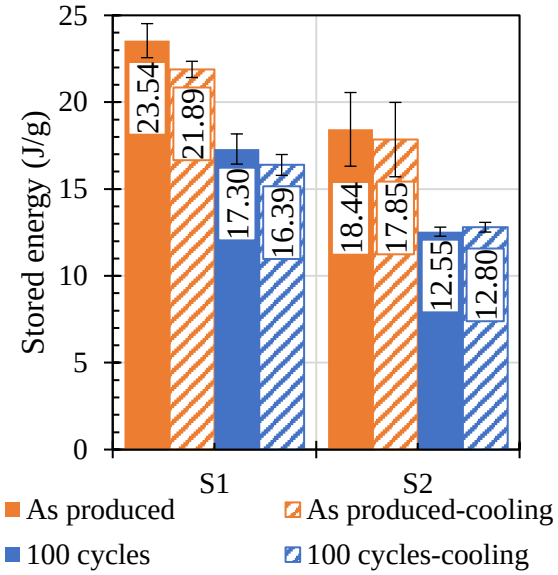

Figure 11. Energy associated to the phase transition (melting and cooling) for each sample before and after thermal cycles simulating service; values are the average of the enthalpy measured in each of the two cycles of the DSC test

3.3.2 Thermal conductivity

The selected areas for the calculation of thermal conductivity with LMC method are shown in Figure 12 for both samples. Ten areas per micrograph were selected, either in regions where Sn particles are elongated and in regions characterized by more isolated Sn particles.

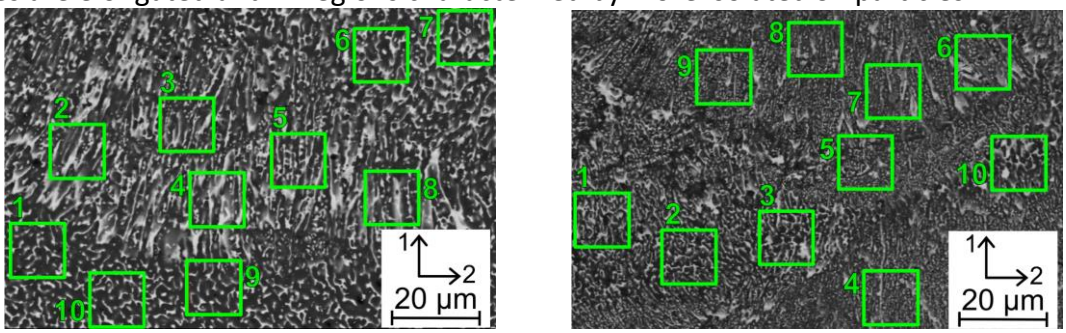

Figure 12. Selected areas for the calculation of thermal conductivity with LMC method for S1 (a) and S2 (b) samples.

To check if the number of jumps suggested by Li [33] for lattices of size 100*100 was suitable to obtain meaningful results for the present microstructures, the simulation was repeated for all areas of S1 sample increasing the number of jumps (5, 100, 1000, 10000) without modifying the other parameters. The trend of the average thermal conductivity as function of jump number (Figure 13) suggests a horizontal asymptote at high values of jump number for most of the curves. According to these results, it seems reasonable to consider thermal conductivity computed with 10000 jumps as the actual value. Therefore, thermal conductivity for S2 sample was computed with this jump number only.

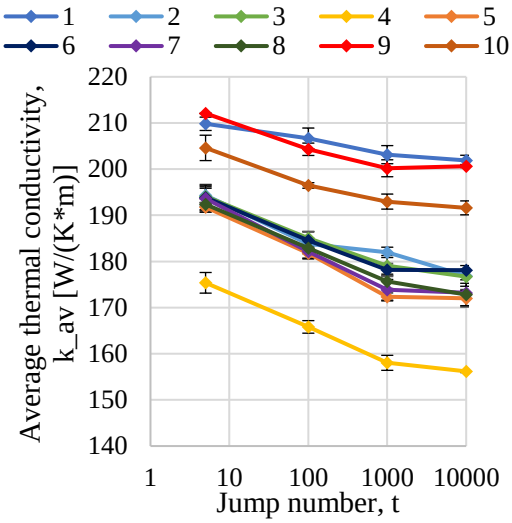

Figure 13. Average thermal conductivity calculated for each area in S1 sample with increasing jump number

Effective thermal conductivity values obtained in each area are presented for S1 sample (Figure 14a) and S2 sample (Figure 14b) as function of the actual Sn content (volume fraction); the reported values are thermal conductivity in direction 1 (parallel to building direction, k_1), in direction 2 (perpendicular to building direction, k_2) and the average between the two directions (k_av). All values lie between the lower and upper bounds defined by the rule of mixtures.

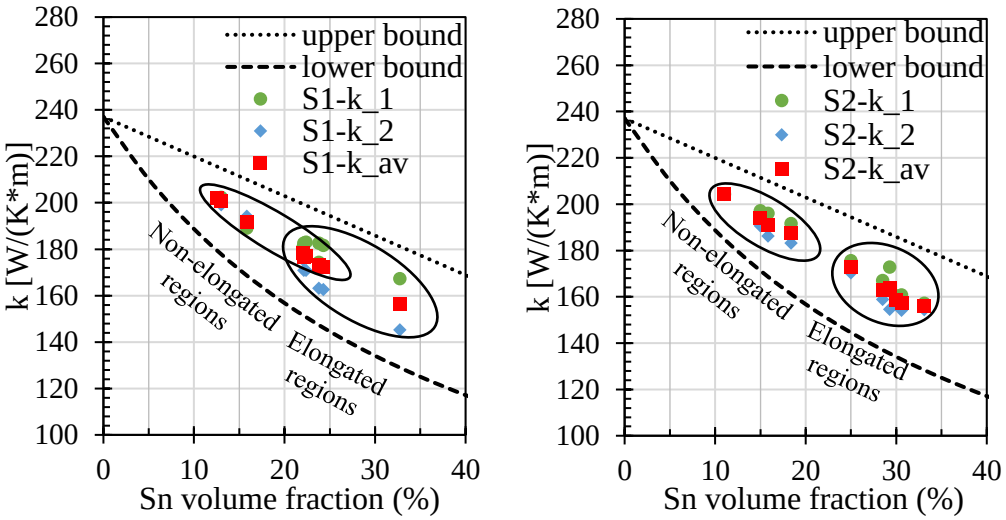

Figure 14. Effective thermal conductivity (in W m^{-1} K^{-1}) of each area in S1 (a) and S2 (b) samples in direction 1 (k_1), in direction 2 (k_2) and average between the two directions (k_av), as function of Sn content in volume fraction. Also, the upper and lower bounds of effective thermal conductivity computed with the rule of mixtures are shown.

For both samples, effective thermal conductivity values ranged from about 150 W m^{-1} K^{-1} to 200 W m^{-1} K^{-1}. Nevertheless, the standard deviation in the three repeated simulation on the same image is generally lower than 1.5%, with a peak of 3.29%. The local Sn volume fraction clearly affects thermal conductivity: higher values of thermal conductivity are found for areas with lower Sn content, corresponding to higher Al content, which is the phase providing the higher thermal conductivity. On the other hand, comparing k_av values for the area 3 with elongated Sn particles in the micrograph and the area 6 with equiaxial Sn particles in S1 sample, both having Sn volume fraction around 22%, average thermal conductivity is almost the same, about 177 W m^{-1} K^{-1}. For S1

sample, the difference between k_1 and k_2 in areas with elongated particles ranges from 6% to more than 13%, while for zones with equiaxial particles it is less than 3%. For the former, the higher conductivity value is found in direction 1, that is the direction in which particles are elongated. Considering S2 sample instead, the difference between conductivities in the two directions is generally below 5%, with only one peak of about 10% in area 4. In this case, the effect of the two kinds of regions (elongated or equiaxial in the micrograph) on the anisotropy of thermal conductivity seems to be less evident.

As far as the overall effective thermal conductivity of the two materials is concerned, the average values of Sn volume fraction and effective thermal conductivity per each sample were computed (Table 2). Considering the standard deviations, either the overall Sn content and the effective thermal conductivity values are close in the two samples. For both, conductivity in building direction (direction 1) is higher than conductivity in direction 2; this difference is slightly bigger for S1 sample: 4.87% with respect to 3.88% for S2 sample.

	Sn volume fraction (v%)	**Effective thermal conductivity [W m^{-1} K^{-1}]**		
		Average (k_av)	**in direction 1 (k_1)**	**in direction 2 (k_2)**
S1	21.24 ± 6.05	180.01 ± 14.12	184.49 ± 10.86	175.52 ± 18.01
S2	23.66 ± 7.87	174.90 ± 17.78	178.36 ± 17.53	171.44 ± 18.37

Table 2. Average values of Sn volume fraction and effective thermal conductivity

4. Discussion

4.1. Microstructural features

The microstructural features observed in the analysed samples and their correlation to the specific manufacturing process have some peculiarities that deserve in-depth consideration: phase distribution, cracks, pores and microstructural changes induced by simulated service. They will be here described separately, even if some aspects are interlinked.

Phase distribution after rapid solidification of both samples resulted, as expected, in a very fine microstructure where Al and Sn are clearly evident. A comparison between these microstructures and the set of microstructures obtained by the authors for the same alloy composition through different powder metallurgy methods showed that the fine size and distribution of the two phases displays some similarities with those obtained by ball-milled powders [4,16] (Figure 15a) than to the coarser simple-mixed ones [15] (Figure 15b). In more detail, focusing the attention on the distribution of Sn phase, to which the PCM effects are correlated, ball-milled samples include both submicrometric particles and slightly elongated particles of a few μm mainly perpendicular to compression direction.

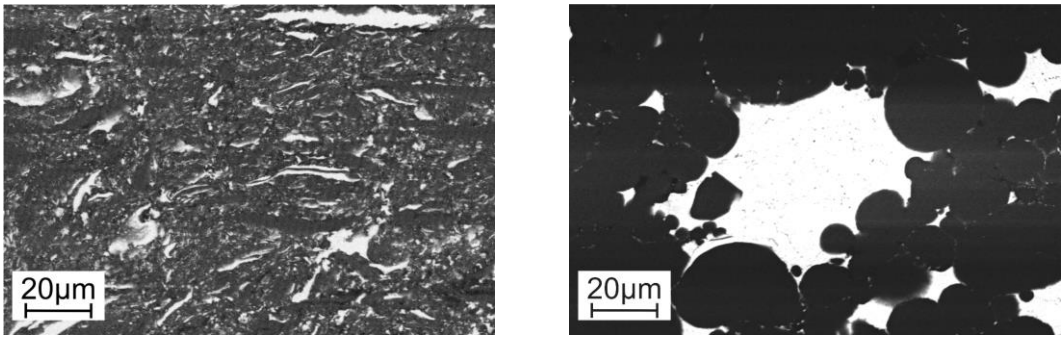

a) b)

Figure 15. Representative microstructural features for Al-40%mass alloy produced by ball-milled or simple-mixed powders then compressed and sintered (a and b, respectively). Both sections are parallel to compression direction (vertical).

In SLM, the coarseness and morphological features of Sn particles are affected by the high cooling rates. In addition, heat flow should be directed mainly downwards along the building direction, toward the Al building platform. Due to its lower specific energy, S2 sampleexperienced a faster cooling and, consequently, its microstructure is generally finer, with smaller and more isolated particles. The elongated Sn particles visible in 2D images of both samples, particularly for specimen S1, are reasonably part of a cellular structure where Sn can be found at boundaries of Al grains growing in an almost parallel manner, as shown in EBSD analysis (Figure 4). In this way, Sn forms an almost interconnected network around Al and the fine distribution cannot create small, isolated Sn particles.

Moreover, the presence of the elongated Sn particles in solidification direction clearly highlights the position of the molten pool regions (Figure 1a). In such cases, it is possible to verify that the distance between two overlaid molten pools is about 20-30 μm, which corresponds approximately to the powder bed layer thickness considering that a layer deposition affects also the layers below ~~of~~ through re-melting or heat treatment. Further, the thin layer which is observed at the boundary of molten pools (identified by dashed line in Figure 2a) is generally richer in Al, with nanometric Sn particles, as result of the early solidification.

In regions where Sn particles do not appear elongated, it is not so easy to distinguish molten pools according to Sn distribution and microstructure is too fine to obtain EBSD images with sufficient quality to verify grain orientations. In order to explain the formation of this microstructure, it is possible to suppose that it resulted from recrystallization of Al and remelting of Sn, due to repeated thermal cycles during deposition of following layers. However, this assumption does not match with the distribution of the regions, which do not occur between every overlaid molten pool, and whose high thickness can correspond to one or even two layers. Therefore, these regions reasonably belong to molten pools, and the absence of elongated grains is due to the angle formed by the cell orientation with the metallographic section plane. According to Underwood [28], 2D structures (elongated grains) can appear like 1D structures (more or less equiaxial grains) on a plane cutting the volume in which they are contained. The shape of the section that is “seen” on the plane (the micrograph) depends on the angle between the particle and the plane itself. SLM deposition can be considered as a series of overlapping welded spots (i.e., solidified molten pools), each of them displaying cellular growth along heat removal directions, which on the farthest regions of the molten pool are oriented almost perpendicularly to the building direction. As a result, cellular structures should appear as highly elongated only when the metallographic section plane cuts the cellular structure along its growth direction, which is the case with cells formed at the centre/bottom of the molten pool, which are elongated on building direction. In all the other cases, cells appear as less elongates or even almost equiaxial structures. Moreover, the used scanning strategy was meander rotated of 67° every layer, therefore when cutting the sample perpendicularly to its surfaces, every molten pool can be sectioned along a different plane, due to both different orientations of the laser path with respect to the cut and the rotation between consecutive layers.

This above interpretation was developed from S1 sample micrographs, but it can be reasonably considered also for S2 sample, where Sn is much finely distributed due to higher solidification rate. Moreover, the higher cooling rate in S2 could also be responsible for the formation of small discontinuities and coarse vertical cracks completely filled by Sn visible at low magnification, that will be considered later. The presence, in both samples, of Sn accumulation in the lower portions of the molten pools, where Al shrinkage is advanced, is ascribed to the Sn network, which prevents a complete isolation of Sn particles allowing its flow when it is molten.

Specifically focusing on cracks, they were observed both before and after service~~,~~ at interfaces between cellular structures and Sn can be found inside them, in higher amount after service. As

reported by DebRoy et al. [39], thermal stresses generally arise in the sample during additive manufacturing production processes. Those stresses are caused by both solidification shrinkage as well as thermal strain due to thermal gradient (relatively high for Al) and all this can lead to crack formation. In addition, the fact that Sn has a much lower solidification temperature (~232°C) with respect to Al (liquidus temperature in Al-40Sn m%: 615.47°C [31,32]) could have played a major role in crack formation, since solid and liquid phase coexist for a relatively long time [40]. According to Saito et al. [41], during solidification of casting Al-Sn alloys, a liquid Sn film forms at the boundary of primary Al grains and rupture can occur in it due to excessive strain/stress caused by shrinkage during solidification. The same mechanism is likely to have occurred during SLM process, as shown in Figure 4b. Moreover, the presence of thermal stresses, small defects, and the above-mentioned cellular structure could have enhanced crack formation. This phenomenon is expected to occur especially where thermal stresses are particularly high (such as those arising perpendicularly to the building direction) and in lower-resistance regions, such as the interfaces between cellular grains vertically elongated (see Figure 6) or within the less resistant Sn phase in cellular structures elongated in the building direction (Figure 4b), where stress transfer to Al phase is not possible.When the region containing a crack is heated up in a later stage of the process, molten tin from the upper parts of the molten pool or from later overlaying molten pools fill the formed gaps which can extend due to thermal stresses. Depending on the actual location of the crack and the presence of previously existing defects, the newly flown Sn can fill cracks or simply broaden the interface between Al cells. The two samples here considered were produced using two different combinations of the parameters selected for the two sets of produced samples, when point distance was decreased, the vertical crack density increased, while the pore size reduced.

The morphological analysis of pores in both cutting directions (parallel and perpendicular to building direction) suggests that they have a nearly spherical shape, with mode aspect ratio ~1.4 and mode circularity 1. Their presence can be due to concurrent causes. The first one is the presence of gas which, in SLM process, could be related to shielding gas, alloy vapours inside molten pool or evaporated moisture initially entrapped in powders [39]. The fact that S1 sample has larger pores with respect to S2 is attributed by the authors to the higher energy density (160 J/mm^3 vs. 128 J/mm^3) which resulted in higher temperature of the melting pool and so higher expansion of entrapped gas volume. Further, some pores showed traces of Sn inside and some Sn particles are spherical: therefore, it is possible that Sn partially or completely filled pores. The formation process could have been the following: during cooling, when the alloy was partially solidified, the reduction of temperature caused a reduction of gas pressure in the pore without significantly changing its volume in the already solidified Al phase; the pressure difference should have allowed molten Sn to flow inside the pore in subsequent steps as the inner pressure reduced. This hypothesis is supported also by the shape of Sn traces inside pores (Figure 3). Moreover, considering EBSD analysis of S1 sample in as-produced conditions, the horizontal elongation of grains observed inside coarse Sn particles suggests that they formed due to the stepwise Sn flow during solidification, otherwise, a mainly vertical grain orientation would be expected according to grain growth along the main cooling direction (parallel to building direction). In addition, high magnification micrographs (Figure 2) showed some pores which are more irregular and are probably due to process issues, like short feed and lack of fusion due to spattering [39]. Lastly, a further reason for Sn filled pores could be the presence of big Sn agglomerates in the powder and that the absence or partial presence of Sn within pores could be due to sample metallographic preparation. The authors have not the possibility to verify these hypothesis.

The presence of pores is of course detrimental to mechanical properties, even if most of them have a spherical shape which is not critical for crack formation. Moreover, porosity affects two of

the major properties of metallic PCMs: high density and high thermal conductivity [5]. The reduction of thermal conductivity was neither tested experimentally nor simulated, but it is strongly expected. Process parameters optimization as well as careful drying of powers should help to reduce porosity. Nevertheless, a small amount of spherical pores ready to be filled by Sn can have a positive effect too, since they can trap molten Sn during phase transition avoiding leakage and reducing stresses caused by solid/liquid expansion of Sn during thermally cycled service of these PCM materials.

As far as the microstructural changes taking place during simulated service are concerned, the experimental results showed that Sn is mostly located at the low-melting and interconnected parts of cellular structure. During simulated service, molten Sn can flow through them towards discontinuities and even toward the external surface. The “beachmarks” observed in section perpendicular to building direction after simulated service (Figure 5) are attributed to the above flow of liquid Sn occurring in every thermal cycle. On one hand, this situation can be positive since Sn can fill pores and/or cracks formed in production process as well as during service. On the other hand, this is detrimental for the possibility of avoiding leakage from the external surface, i.e., the structure is not “form-stable”.

4.2. Mechanical properties

In as-produced conditions, hardness of the S1 sample is about 28% lower than the one of S2 sample. This significant difference mainly results from the finer microstructure of S2 even if the role of porosity in the first sample cannot be neglected. The finer microstructure of S2 sample also revealed the presence of isolated Sn particles of sub-micrometric size. Accordingly to Liu et al. dispersion-hardening strengthening effect can be obtained when homogeneous distribution of Sn nanoparticles in nanocrystalline Al matrix occurs, in contrast with the presence of Sn network around Al grains [13].

Focusing on standard deviation of average hardness values, both samples have a standard deviation around 10% of the hardness value, with a peak of more than 40% for sample S1 after 100 cycles. These significant variations can be ascribed to the greater presence of defects (i.e., porosities and cracks) and different local microstructures, that can reduce or increase the hardness value pointwise. As a matter of fact, regions with different microstructures are generally indistinguishable using an optical microscope; therefore, during the microhardness test, it not possible to know exactly where the indentation is done.

After simulated service, S2 sample shows a decrease in hardness of about 30% after thermal cycles, while the average hardness of S1 can be considered constant. However, S1 sample has a wide standard deviation and, if its average hardness is computed excluding the highest measured values, a hardness reduction of 28% is found. As shown before, during thermal cycles, this sample underwent microstructural changes with the formation of Sn-rich and Sn-poor regions. Therefore, a wider hardness scattering results for serviced samples.

The above hardness values can be considered for a comparison between the samples investigated in the present paper and those of samples produced with other methods. While hardness of S1 sample in different conditions are fully within the range of cast Al-Sn alloys, i.e. ~30 HV [14], those of S2 sample are similar to the ones obtained in a previous study of the authors using powder metallurgy process with simple mixed powders. Here, values of about 40 HV in as produced conditions reduce to 30 HV after simulated service [15].

On the other hand, hardness values of both samples are significantly lower than the ones obtained by Liu et al. [14] using powder metallurgy (ball milling), i.e. ~90HV, and the ones obtained by Ning et al. [17] using cold spray, i.e. ~70HV. With respect to the works by Liu et al. [13. 14], the microstructure of the presently obtained samples does not include extensive homogeneous

dispersion of Sn, and the presence of defects further decreases the average sample hardness. An improvement of the hardness of these Al-20Sn (volume %) alloys produced by SLM process to meet the properties observed for the same alloy obtained with different production methods [4,16,42] could be achieved by process optimization in view of defect reduction and increase of the amount of isolated Sn nanoparticles.

4.3. Thermal behaviour

Even if for PCM materials classically designed for thermal storage devices latent heat of melting is the most important parameter, manufacturing processes can also lead to microstructures where the thermal conductivity can be slightly modified and show some degree of anisotropy. The metallographic analyses of phase distribution associated to LMC simulations clearly showed the inhomogeneity in the Sn amount in different regions of the sample. As far as the thermal conductivity is concerned, regions with particles "oriented" in the solidification direction result in anisotropic thermal conductivity, with higher conductivity along Al grain growth direction. This is particularly evident in S1 sample which has a more significantly oriented microstructure, while the effect is minimal for S2 sample. In conclusion, LMC simulations of effective thermal conductivity confirm that the SLM sample microstructure can affect the thermal response of the system. Although further numerical and experimental studies are required, the present results suggest that fine combination of phases as well as this anisotropy in building direction obtainable with SLM could be considered to promote or inhibit heat flow in specific directions.

Thermal response of the material, is analogous to the ones observed for powder metallurgy Al-Sn alloys in previous studies [4,16,42]: a single narrow peak or two close overlapping peaks in melting at about 230°C and multiple peaks in cooling spanning a relatively wide temperature range. The presence of two close overlapping peaks in melting after simulated service is due to eutectic reaction occurring at a slightly lower temperature with respect to pure Sn melting (228°C, [43]). Regarding the thermal energy associated to these peaks, the latent heat measured for S1 sample is higher than the value obtained for S2 sample, the former being almost equal to the theoretical value for an Al-Sn alloy containing 20% of Sn in volume (23.6 J/g). As shown by Perrin and Gariboldi [15], the thermal energy stored in Al-Sn alloys due to Sn melting is directly proportional to the actual Sn content in the sample. Even if there are no reasons to expect an overall sample composition different from the initial powder blend (i.e., 20% volume of Sn), micrographs and especially LMC analysis showed that Sn fraction varies locally inside the sample regions. In more detail, Sn volume in LMC areas ranged from 11% to 33% in volume corresponding to a computed latent heat between 15 J/g and 34 J/g; experimental energy values for both samples fall in this range. Therefore, in the present DSC analysis, it is more interesting to consider peak positions and relative latent heat values, than the exact values which are dependent on the selected volume in the sample. Nevertheless, the reduction of stored energy after thermal cycles simulating service (~30% for both samples) is supposed to be significantly affected also by the observed Sn leakage (par. 4.1).

Further, the fact that the sum of all solidification peaks is almost equal to the melting peak proves that all the peaks observed in cooling are related to Sn solidification. The explanation for this behaviour involves the occurrence of undercooling. Undercooling is a metastable state in which a material remains liquid when cooled below its melting point temperature and it is generally taken ~~onto~~ into account in PCM applications, such as in salt hydrates [44,45]. This happens when the spontaneous formation of the thermodynamically stable solid phase is prevented by a nucleation barrier [44]. During the initial cooling process, a part of the heat is released (first peak), but the remaining phase transition energy can be stored for extended periods of time (even hours for salt hydrates) without further loss of energy [45]. In the case of Al-Sn alloy, undercooling can happen

because Sn does not wet Al well, so there are few sites for heterogeneous nucleation, hindering the overall nucleation [44]; this situation occurs both inside the alloy and when Sn powders are tested, since the crucible is made of Al (see par. 3.3.1). Studies about heterogeneous nucleation of Sn particles in Al matrix proved that solidification depends on the specific nucleation site, that is on the interfacial energy between the particle and the substrate or matrix [46]. Kim and Cantor [22] and Zhang et al. [23] demonstrated that solidification peaks with a low undercooling (onset temperature around 220°C) are associated to bulk or micrometric Sn particles, while peaks at lower temperature are characteristic of Sn particles embedded in Al matrix. In the presented samples, embedded particles are present, although they are relatively few, and, consequently, they have short peaks at low temperature. According to Singh et al. [46], being in contact with several matrix grains, each particle can have more than one possible nucleation site that is kinetically selected: so, in repeated thermal cycles, a particle can solidify with different orientation every time, resulting in the little variations observed in DSC peaks in different cycles.

5. Conclusions

In the present paper, a first attempt of producing Al-Sn alloys using rapid solidification through Selective Laser Melting was carried out in view of its application as composite Phase Change Material. This approach resulted in an extremely fine microstructure, providing a thermal response similar to the one obtained with samples with fine microstructure previously produced by powder metallurgy. Mechanical properties, evaluated through Vickers microhardness, are close to properties obtained in casting and simple powder metallurgy processes. This process proved to have a good potentiality to produce composite metallic PCMs, since this technique can overcome complexity and geometrical limitations faced in powder metallurgy processes keeping comparable properties. A certain degree of anisotropy along the building direction has been observed for microstructural features as well as for thermal conductivity. A careful optimization of process parameters, and maybe of matrix composition too, should help to reduce the presence of macroscopic defects, with beneficial effect on mechanical properties and thermal stability

Acknowledgments

The authors would like to thank Maria Rosaria Pagano (Department of Aerospace Science and Technology, Politecnico di Milano) for conducting the DSC tests and prof. Riccardo Casati (Department of Mechanical Engineering, Politecnico di Milano) for his help in material production.

The Italian Ministry of Education, University and Research is acknowledged for the support through the Project “Department of Excellence LIS4.0−Lightweight and Smart Structures for Industry 4.0”.

Author contributions

Chiara Confalonieri: Methodology, Investigation, Formal analysis, Writing – Original Draft, Writing – Review and Editing.
Elisabetta Gariboldi: Conceptualization, Methodology, Investigation, Writing – Review and Editing.

Declaration of interests

None.

Data availability

The raw data required to reproduce these findings cannot be shared at this time as the data also forms part of an ongoing study. The processed data required to reproduce these findings cannot be shared at this time as the data also forms part of an ongoing study.

References

[1] A.S. Fleischer, Thermal Energy Storage Using Phase Change Materials - Fundamentals and Applications, 1st ed., Springer, Cham, 2015. doi:https://doi.org/10.1007/978-3-319-20922-7.

[2] G. Wei, G. Wang, C. Xu, X. Ju, L. Xing, X. Du, Y. Yang, Selection principles and thermophysical properties of high temperature phase change materials for thermal energy storage: A review, Renew. Sustain. Energy Rev. 81 (2018) 1771–1786. doi:10.1016/J.RSER.2017.05.271.

[3] S.A. Mohamed, F.A. Al-Sulaiman, N.I. Ibrahim, M.H. Zahir, A. Al-Ahmed, R. Saidur, B.S. Yılbaş, A.Z. Sahin, A review on current status and challenges of inorganic phase change materials for thermal energy storage systems, Renew. Sustain. Energy Rev. 70 (2017) 1072–1089. doi:10.1016/J.RSER.2016.12.012.

[4] C. Confalonieri, A.T. Grimaldi, E. Gariboldi, Ball-milled Al–Sn alloy as composite Phase Change Material, Mater. Today Energy. 17 (2020) 100456. doi:10.1016/j.mtener.2020.100456.

[5] C. Zhou, S. Wu, Medium- and high-temperature latent heat thermal energy storage: Material database, system review, and corrosivity assessment, Int. J. Energy Res. 43 (2019) 621–661. doi:10.1002/er.4216.

[6] W. Su, J. Darkwa, G. Kokogiannakis, Review of solid–liquid phase change materials and their encapsulation technologies, Renew. Sustain. Energy Rev. 48 (2015) 373–391. doi:https://doi.org/10.1016/j.rser.2015.04.044.

[7] E. Gariboldi, L.P.M. Colombo, D. Fagiani, Z. Li, Methods to Characterize Effective Thermal Conductivity, Diffusivity and Thermal Response in Different Classes of Composite Phase Change Materials, Materials (Basel). 12 (2019) 2552. doi:10.3390/ma12162552.

[8] K. Pielichowska, K. Pielichowski, Phase change materials for thermal energy storage, Prog. Mater. Sci. 65 (2014) 67–123. doi:10.1016/J.PMATSCI.2014.03.005.

[9] H. Sugo, E. Kisi, D. Cuskelly, Miscibility gap alloys with inverse microstructures and high thermal conductivity for high energy density thermal storage applications, Appl. Therm. Eng. 51 (2013) 1345–1350. doi:10.1016/J.APPLTHERMALENG.2012.11.029.

[10] T. Stuczyñski, Metallurgical problems associated with the production of aluminium-tin alloys, Mater. Des. 18 (1997) 369–372. doi:https://doi.org/10.1016/S0261-3069(97)00078-2.

[11] X. Liu, M.Q. Zeng, Y. Ma, M. Zhu, Wear behavior of Al–Sn alloys with different distribution of Sn dispersoids manipulated by mechanical alloying and sintering, Wear. 265 (2008) 1857–1863. doi:10.1016/J.WEAR.2008.04.050.

[12] Z.C. Lu, M.Q. Zeng, Y. Gao, M. Zhu, Significant improvement of wear properties by creating micro/nano dual-scale structure in Al–Sn alloys, Wear. 296 (2012) 469–478. doi:https://doi.org/10.1016/j.wear.2012.08.002.

[13] X. Liu, M.Q. Zeng, Y. Ma, M. Zhu, Melting behavior and the correlation of Sn distribution on hardness in a nanostructured Al–Sn alloy, Mater. Sci. Eng. A. 506 (2009) 1–7. doi:10.1016/J.MSEA.2008.12.054.

[14] X. Liu, M.Q. Zeng, Y. Ma, M. Zhu, Promoting the high load-carrying capability of Al–20wt%Sn bearing alloys through creating nanocomposite structure by mechanical alloying, Wear.

294–295 (2012) 387–394. doi:10.1016/j.wear.2012.07.021.
[15] E. Gariboldi, M. Perrin, Metallic Composites as Form-Stable Phase Change Alloys, Mater. Sci. Forum. 941 (2018) 1966–1971. doi:10.4028/www.scientific.net/MSF.941.1966.
[16] C. Confalonieri, P. Bassani, E. Gariboldi, Microstructural and thermal response evolution of metallic form-stable phase change materials produced from ball-milled powders, J. Therm. Anal. Calorim. 142 (2020) 85–96. doi:10.1007/s10973-020-09785-7.
[17] X.-J. Ning, J.-H. Kim, H.-J. Kim, C. Lee, Characteristics and heat treatment of cold-sprayed Al–Sn binary alloy coatings, Appl. Surf. Sci. 255 (2009) 3933–3939. doi:https://doi.org/10.1016/j.apsusc.2008.10.074.
[18] O.A. Chikova, A.N. Konstantinov, E. V Shishkina, D.S. Chezganov, Nanoindentation study of the effect of the structural state of the melt on the crystal structure and mechanical properties of the phases in an Al-50 wt % Sn alloy, Russ. Metall. 2013 (2013) 535–544. doi:10.1134/S0036029513070045.
[19] M.E. Makhatha, O.S. Fatoba, E.T. Akinlabi, Effects of rapid solidification on the microstructure and surface analyses of laser-deposited Al-Sn coatings on AISI 1015 steel, Int. J. Adv. Manuf. Technol. 94 (2018) 773–787. doi:10.1007/s00170-017-0876-y.
[20] T. Marrocco, L.C. Driver, S.J. Harris, D.G. McCartney, Microstructure and properties of thermally sprayed Al-Sn-based alloys for plain bearing applications, J. Therm. Spray Technol. 15 (2006) 634–639. doi:10.1361/105996306X147009.
[21] M.C. Lucchetta, F. Saporiti, F. Audebert, Improvement of surface properties of an Al–Sn–Cu plain bearing alloy produced by rapid solidification, J. Alloys Compd. 805 (2019) 709–717. doi:10.1016/j.jallcom.2019.07.082.
[22] W.T. Kim, B. Cantor, Solidification of tin droplets embedded in an aluminium matrix, J. Mater. Sci. 26 (1991) 2868–2878. doi:10.1007/BF01124815.
[23] W. Zhang, B. Zhao, Q. Zhai, Y. Gao, Application of fast scanning calorimetry in the rapid solidification of tin particles embedded in Al matrix, in: Miner. Met. Mater. Soc. 2013 142nd Annu. Meet. Exhib. Annu. Meet. Suppl. Proc., John Wiley & Sons, Incorporated, 2013: pp. 477–484. https://ebookcentral.proquest.com/lib/polimi/detail.action?docID=1157727#.
[24] Z. Zhang, Y. Wang, X. Bian, W. Wang, Orientation of nanocrystals in rapidly solidified Al-based alloys and its correlation to the compound-forming tendency of alloys, J. Cryst. Growth. 281 (2005) 646–653. doi:10.1016/j.jcrysgro.2005.04.052.
[25] C. Confalonieri, M. Perrin, E. Gariboldi, Combined powder metallurgy routes to improve thermal and mechanical response of Al−Sn composite phase change materials, Trans. Nonferrous Met. Soc. China. 30 (2020) 3226–3239. doi:https://doi.org/10.1016/S1003-6326(20)65456-5.
[26] C. Confalonieri, Innovative methods to produce and characterize metallic Phase Change Materials, Politecnico di Milano, 2018.
[27] W.S. Rasband, ImageJ, (2018). https://imagej.net/Welcome.
[28] E.E. Underwood, The Mathematical Foundations of Quantitative Stereology, in: G. Pellissier, S. Purdy (Eds.), Stereol. Quant. Metallogr., ASTM International, West Conshohocken, PA, 1972: pp. 3–38. doi:10.1520/STP36841S.
[29] T. Ferreira, W. Rasband, ImageJ User Guide, (2012). https://imagej.nih.gov/ij/docs/guide/146.html (accessed November 25, 2019).
[30] Y. Takashimizu, M. Iiyoshi, New parameter of roundness R: circularity corrected by aspect ratio, Prog. Earth Planet. Sci. 3 (2016) 2. doi:10.1186/s40645-015-0078-x.
[31] Thermo-Calc Software TCAL5.1 Al-alloys database, (n.d.).
[32] J.-O. Andersson, T. Helander, L. Höglund, P. Shi, B. Sundman, Thermo-Calc & DICTRA, computational tools for materials science, Calphad. 26 (2002) 273–312.

doi:https://doi.org/10.1016/S0364-5916(02)00037-8.
[33] Z. Li, E. Gariboldi, Reliable estimation of effective thermal properties of a 2-phase material by its optimized modelling in view of Lattice Monte-Carlo simulation, Comput. Mater. Sci. 169 (2019) 109–125. doi:https://doi.org/10.1016/j.commatsci.2019.109125.
[34] Z. Li, C. Confalonieri, E. Gariboldi, Numerical and Experimental Evaluation of Thermal Conductivity: An Application to Al-Sn Alloys, Met. 2021, Vol. 11, Page 650. 11 (2021) 650. doi:10.3390/MET11040650.
[35] A. Rawson, E. Kisi, H. Sugo, T. Fiedler, Effective conductivity of Cu–Fe and Sn–Al miscibility gap alloys, Int. J. Heat Mass Transf. 77 (2014) 395–405. doi:10.1016/J.IJHEATMASSTRANSFER.2014.05.024.
[36] N. Otsu, A Threshold Selection Method from Gray-Level Histograms, IEEE Trans. Syst. Man. Cybern. 9 (1979) 62–66.
[37] F. Cardarelli, F. Cardarelli, Common Nonferrous Metals, in: Mater. Handb. A Concise Deskt. Ref., 2nd ed., Springer London, Limited, London, UNITED KINGDOM, 2008: pp. 159–212. http://ebookcentral.proquest.com/lib/polimi/detail.action?docID=372240.
[38] T. Fiedler, I.V. Belova, G.E. Murch, Theoretical and Lattice Monte Carlo analyses on thermal conduction in cellular metals, Comput. Mater. Sci. 50 (2010) 503–509. doi:10.1016/j.commatsci.2010.09.011.
[39] T. DebRoy, H.L. Wei, J.S. Zuback, T. Mukherjee, J.W. Elmer, J.O. Milewski, A.M. Beese, A. Wilson-Heid, A. De, W. Zhang, Additive manufacturing of metallic components – Process, structure and properties, Prog. Mater. Sci. 92 (2018) 112–224. doi:https://doi.org/10.1016/j.pmatsci.2017.10.001.
[40] J. Liu, S. Kou, Crack susceptibility of binary aluminum alloys during solidification, Acta Mater. 110 (2016) 84–94. doi:https://doi.org/10.1016/j.actamat.2016.03.030.
[41] Y. Saito, H. Todoroki, Y. Kobayashi, N. Shiga, S.-I. Tanaka, Hot-Cracking Mechanism in Al–Sn Alloys from a Viewpoint of Measured Residual Stress Distributions, Mater. Trans. 59 (2018) 908–916. doi:10.2320/matertrans.M2018011.
[42] C. Confalonieri, Z. Li, E. Gariboldi, Metallic Form-Stable Phase Change Materials for Thermal Energy Storage and Management: general features and effect of manufacturing process on thermal response and stability, La Metall. Ital. - Int. J. Ital. Assoc. Metall. 7/8 (2019) 12–20.
[43] A.J. McAlister, D.J. Kahan, The Al−Sn (Aluminum-Tin) System, Bull. Alloy Phase Diagrams. 4 (1983) 410–414. doi:10.1007/BF02868095.
[44] A. Safari, R. Saidur, F.A. Sulaiman, Y. Xu, J. Dong, A review on supercooling of Phase Change Materials in thermal energy storage systems, Renew. Sustain. Energy Rev. 70 (2017) 905–919. doi:https://doi.org/10.1016/j.rser.2016.11.272.
[45] B. Sandnes, J. Rekstad, Supercooling salt hydrates: Stored enthalpy as a function of temperature, Sol. Energy. 80 (2006) 616–625. doi:https://doi.org/10.1016/j.solener.2004.11.014.
[46] A. Singh, H. Somekawa, Y. Matsushita, A.P. Tsai, Solidification of tin on quasicrystalline surfaces, Philos. Mag. 92 (2012) 1106–1128. doi:10.1080/14786435.2011.640646.